

See discussions, stats, and author profiles for this publication at: <https://www.researchgate.net/publication/232238239>

Search for Neutrinos from Annihilating Dark Matter in the Direction of the Galactic Center with the 40-String IceCube Neutrino Observatory

Article · October 2012

Source: arXiv

CITATIONS

19

READS

98

271 authors, including:



Yasser Abdou
Tanta University

133 PUBLICATIONS 4,968 CITATIONS

[SEE PROFILE](#)



Juan Antonio Aguilar Sánchez
Université Libre de Bruxelles

376 PUBLICATIONS 12,813 CITATIONS

[SEE PROFILE](#)



David Altmann
Humboldt-Universität zu Berlin

182 PUBLICATIONS 8,026 CITATIONS

[SEE PROFILE](#)



Karen Andeen
Marquette University

227 PUBLICATIONS 9,312 CITATIONS

[SEE PROFILE](#)

Some of the authors of this publication are also working on these related projects:



XENON Dark Matter [View project](#)



Strongly correlated Fermi systems as a new state of matter [View project](#)

Search for Neutrinos from Annihilating Dark Matter in the Direction of the Galactic Center with the 40-String IceCube Neutrino Observatory

R. Abbasi,²⁷ Y. Abdou,²² M. Ackermann,⁴¹ J. Adams,¹⁵ J. A. Aguilar,²¹ M. Ahlers,²⁷ D. Altmann,⁹ K. Andeen,²⁷ J. Auffenberg,²⁷ X. Bai,^{31,*} M. Baker,²⁷ S. W. Barwick,²³ V. Baum,²⁸ R. Bay,⁷ K. Beattie,⁸ J. J. Beatty,^{17,18} S. Bechet,¹² J. Becker Tjus,¹⁰ K.-H. Becker,⁴⁰ M. Bell,³⁸ M. L. Benabderrahmane,⁴¹ S. BenZvi,²⁷ J. Berdermann,⁴¹ P. Berghaus,⁴¹ D. Berley,¹⁶ E. Bernardini,⁴¹ D. Bertrand,¹² D. Z. Besson,²⁵ D. Bindig,⁴⁰ M. Bissok,¹ E. Blaufuss,¹⁶ J. Blumenthal,¹ D. J. Boersma,^{39,1} C. Boehm,³⁴ D. Bose,¹³ S. Böser,¹¹ O. Botner,³⁹ L. Brayeur,¹³ A. M. Brown,¹⁵ R. Bruijn,²⁴ J. Brunner,⁴¹ M. Carson,²² J. Casey,⁵ M. Casier,¹³ D. Chirkin,²⁷ B. Christy,¹⁶ K. Clark,³⁸ F. Clevermann,¹⁹ S. Cohen,²⁴ D. F. Cowen,^{38,37} A. H. Cruz Silva,⁴¹ M. Danninger,³⁴ J. Daughhetee,⁵ J. C. Davis,¹⁷ C. De Clercq,¹³ S. De Ridder,²² F. Descamps,²⁷ P. Desiati,²⁷ G. de Vries-Uiterweerd,²² T. DeYoung,³⁸ J. C. Díaz-Vélez,²⁷ J. Dreyer,¹⁰ J. P. Dumm,²⁷ M. Dunkman,³⁸ R. Eagan,³⁸ J. Eisch,²⁷ R. W. Ellsworth,¹⁶ O. Engdegård,³⁹ S. Euler,¹ P. A. Evenson,³¹ O. Fadiran,²⁷ A. R. Fazely,⁶ A. Fedynitch,¹⁰ J. Feintzeig,²⁷ T. Feusels,²² K. Filimonov,⁷ C. Finley,³⁴ T. Fischer-Wasels,⁴⁰ S. Flis,³⁴ A. Franckowiak,¹¹ R. Franke,⁴¹ K. Frantzen,¹⁹ T. Fuchs,¹⁹ T. K. Gaisser,³¹ J. Gallagher,²⁶ L. Gerhardt,^{8,7} L. Gladstone,²⁷ T. Glüsenskamp,⁴¹ A. Goldschmidt,⁸ G. Golup,¹³ J. A. Goodman,¹⁶ D. Góra,⁴¹ D. Grant,²⁰ A. Groß,³⁰ S. Grullon,²⁷ M. Gurtner,⁴⁰ C. Ha,^{8,7} A. Haj Ismail,²² A. Hallgren,³⁹ F. Halzen,²⁷ K. Hanson,¹² D. Heereman,¹² P. Heimann,¹ D. Heinen,¹ K. Helbing,⁴⁰ R. Hellauer,¹⁶ S. Hickford,¹⁵ G. C. Hill,² K. D. Hoffman,¹⁶ R. Hoffmann,⁴⁰ A. Homeier,¹¹ K. Hoshina,²⁷ W. Huelsnitz,^{16,†} J.-P. Hülß,¹ P. O. Hulth,³⁴ K. Hultqvist,³⁴ S. Hussain,³¹ A. Ishihara,¹⁴ E. Jacobi,⁴¹ J. Jacobsen,²⁷ G. S. Japaridze,⁴ O. Jlelati,²² A. Kappes,⁹ T. Karg,⁴¹ A. Karle,²⁷ J. Kiryluk,³⁵ F. Kislat,⁴¹ J. Kläs,⁴⁰ S. R. Klein,^{8,7} J.-H. Köhne,¹⁹ G. Kohnen,²⁹ H. Kolanoski,⁹ L. Köpke,²⁸ C. Kopper,²⁷ S. Kopper,⁴⁰ D. J. Koskinen,³⁸ M. Kowalski,¹¹ M. Krasberg,²⁷ G. Kroll,²⁸ J. Kunnen,¹³ N. Kurahashi,²⁷ T. Kuwabara,³¹ M. Labare,¹³ K. Laihem,¹ H. Landsman,²⁷ M. J. Larson,³⁶ R. Lauer,⁴¹ M. Lesiak-Bzdak,³⁵ J. Lünemann,²⁸ J. Madsen,³³ R. Maruyama,²⁷ K. Mase,¹⁴ H. S. Matis,⁸ F. McNally,²⁷ K. Meagher,¹⁶ M. Merck,²⁷ P. Mészáros,^{37,38} T. Meures,¹² S. Miarecki,^{8,7} E. Middell,⁴¹ N. Milke,¹⁹ J. Miller,¹³ L. Mohrmann,⁴¹ T. Montaruli,^{21,‡} R. Morse,²⁷ S. M. Movit,³⁷ R. Nahnhauser,⁴¹ U. Naumann,⁴⁰ S. C. Nowicki,²⁰ D. R. Nygren,⁸ A. Obertacke,⁴⁰ S. Odrowski,³⁰ A. Olivas,¹⁶ M. Olivo,¹⁰ A. O'Murchadha,¹² S. Panknin,¹¹ L. Paul,¹ J. A. Pepper,³⁶ C. Pérez de los Heros,³⁹ D. Pieloth,¹⁹ N. Pirk,⁴¹ J. Posselt,⁴⁰ P. B. Price,⁷ G. T. Przybylski,⁸ L. Rädcl,¹ K. Rawlins,³ P. Redl,¹⁶ E. Resconi,³⁰ W. Rhode,¹⁹ M. Ribordy,²⁴ M. Richman,¹⁶ B. Riedel,²⁷ J. P. Rodrigues,²⁷ F. Rothmaier,²⁸ C. Rott,¹⁷ T. Ruhe,¹⁹ B. Ruzybayev,³¹ D. Ryckbosch,²² S. M. Saba,¹⁰ T. Salameh,³⁸ H.-G. Sander,²⁸ M. Santander,²⁷ S. Sarkar,³² K. Schatto,²⁸ M. Scheel,¹ F. Scheriau,¹⁹ T. Schmidt,¹⁶ M. Schmitz,¹⁹ S. Schoenen,¹ S. Schöneberg,¹⁰ L. Schönherr,¹ A. Schönwald,⁴¹ A. Schukraft,¹ L. Schulte,¹¹ O. Schulz,³⁰ D. Seckel,³¹ S. H. Seo,³⁴ Y. Sestayo,³⁰ S. Seunarine,³³ M. W. E. Smith,³⁸ M. Soiron,¹ D. Soldin,⁴⁰ G. M. Spiczak,³³ C. Spiering,⁴¹ M. Stamatikos,^{17,§} T. Stanev,³¹ A. Stasik,¹¹ T. Stezelberger,⁸ R. G. Stokstad,⁸ A. Stöbl,⁴¹ E. A. Strahler,¹³ R. Ström,³⁹ G. W. Sullivan,¹⁶ H. Taavola,³⁹ I. Taboada,⁵ A. Tamburro,³¹ S. Ter-Antonyan,⁶ S. Tilav,³¹ P. A. Toale,³⁶ S. Toscano,²⁷ M. Usner,¹¹ D. van der Drift,^{8,7} N. van Eijndhoven,¹³ A. Van Overloop,²² J. van Santen,²⁷ M. Vehring,¹ M. Voge,¹¹ M. Vraeghe,²² C. Walck,³⁴ T. Waldenmaier,⁹ M. Wallraff,¹ M. Walter,⁴¹ R. Wasserman,³⁸ Ch. Weaver,²⁷ C. Wendt,²⁷ S. Westerhoff,²⁷ N. Whitehorn,²⁷ K. Wiebe,²⁸ C. H. Wiebusch,¹ D. R. Williams,³⁶ H. Wissing,¹⁶ M. Wolf,³⁴ T. R. Wood,²⁰ K. Woschnagg,⁷ C. Xu,³¹ D. L. Xu,³⁶ X. W. Xu,⁶ J. P. Yanez,⁴¹ G. Yodh,²³ S. Yoshida,¹⁴ P. Zarzhitsky,³⁶ J. Ziemann,¹⁹ A. Zilles,¹ and M. Zoll³⁴

¹III. Physikalisches Institut, RWTH Aachen University, D-52056 Aachen, Germany

²School of Chemistry & Physics, University of Adelaide, Adelaide SA, 5005 Australia

³Dept. of Physics and Astronomy, University of Alaska Anchorage,
3211 Providence Dr., Anchorage, AK 99508, USA

⁴CTSPS, Clark-Atlanta University, Atlanta, GA 30314, USA

⁵School of Physics and Center for Relativistic Astrophysics,
Georgia Institute of Technology, Atlanta, GA 30332, USA

⁶Dept. of Physics, Southern University, Baton Rouge, LA 70813, USA

⁷Dept. of Physics, University of California, Berkeley, CA 94720, USA

⁸Lawrence Berkeley National Laboratory, Berkeley, CA 94720, USA

⁹Institut für Physik, Humboldt-Universität zu Berlin, D-12489 Berlin, Germany

¹⁰Fakultät für Physik & Astronomie, Ruhr-Universität Bochum, D-44780 Bochum, Germany

¹¹Physikalisches Institut, Universität Bonn, Nussallee 12, D-53115 Bonn, Germany

¹²Université Libre de Bruxelles, Science Faculty CP230, B-1050 Brussels, Belgium

¹³Vrije Universiteit Brussel, Dienst ELEM, B-1050 Brussels, Belgium

¹⁴Dept. of Physics, Chiba University, Chiba 263-8522, Japan

- ¹⁵Dept. of Physics and Astronomy, University of Canterbury, Private Bag 4800, Christchurch, New Zealand
¹⁶Dept. of Physics, University of Maryland, College Park, MD 20742, USA
¹⁷Dept. of Physics and Center for Cosmology and Astro-Particle Physics, Ohio State University, Columbus, OH 43210, USA
¹⁸Dept. of Astronomy, Ohio State University, Columbus, OH 43210, USA
¹⁹Dept. of Physics, TU Dortmund University, D-44221 Dortmund, Germany
²⁰Dept. of Physics, University of Alberta, Edmonton, Alberta, Canada T6G 2G7
²¹Département de physique nucléaire et corpusculaire, Université de Genève, CH-1211 Genève, Switzerland
²²Dept. of Physics and Astronomy, University of Gent, B-9000 Gent, Belgium
²³Dept. of Physics and Astronomy, University of California, Irvine, CA 92697, USA
²⁴Laboratory for High Energy Physics, École Polytechnique Fédérale, CH-1015 Lausanne, Switzerland
²⁵Dept. of Physics and Astronomy, University of Kansas, Lawrence, KS 66045, USA
²⁶Dept. of Astronomy, University of Wisconsin, Madison, WI 53706, USA
²⁷Dept. of Physics and Wisconsin IceCube Particle Astrophysics Center, University of Wisconsin, Madison, WI 53706, USA
²⁸Institute of Physics, University of Mainz, Staudinger Weg 7, D-55099 Mainz, Germany
²⁹Université de Mons, 7000 Mons, Belgium
³⁰T.U. Munich, D-85748 Garching, Germany
³¹Bartol Research Institute and Department of Physics and Astronomy, University of Delaware, Newark, DE 19716, USA
³²Dept. of Physics, University of Oxford, 1 Keble Road, Oxford OX1 3NP, UK
³³Dept. of Physics, University of Wisconsin, River Falls, WI 54022, USA
³⁴Oskar Klein Centre and Dept. of Physics, Stockholm University, SE-10691 Stockholm, Sweden
³⁵Department of Physics and Astronomy, Stony Brook University, Stony Brook, NY 11794-3800, USA
³⁶Dept. of Physics and Astronomy, University of Alabama, Tuscaloosa, AL 35487, USA
³⁷Dept. of Astronomy and Astrophysics, Pennsylvania State University, University Park, PA 16802, USA
³⁸Dept. of Physics, Pennsylvania State University, University Park, PA 16802, USA
³⁹Dept. of Physics and Astronomy, Uppsala University, Box 516, S-75120 Uppsala, Sweden
⁴⁰Dept. of Physics, University of Wuppertal, D-42119 Wuppertal, Germany
⁴¹DESY, D-15735 Zeuthen, Germany

A search for muon neutrinos from dark matter annihilations in the Galactic Center region has been performed with the 40-string configuration of the IceCube Neutrino Observatory using data collected in 367 days of live-time starting in April 2008. The observed fluxes were consistent with the atmospheric background expectations. Upper limits on the self-annihilation cross-section are obtained for dark matter particle masses ranging from 100 GeV to 10 TeV. In the case of decaying dark matter, lower limits on the lifetime have been determined for masses between 200 GeV and 20 TeV.

PACS numbers: 95.35.+d, 98.70.Sa, 96.50.S-, 96.50.Vg

A. Introduction

There is well-established observational evidence for the existence of a non-baryonic cold dark matter component in the universe. Although the exact nature of dark matter remains unknown, many theories beyond the Standard Model of particle physics accommodate stable or extremely long-lived particles as potential dark matter candidates [1]. A favored hypothesis is WIMPs (Weakly Interacting Massive Particles), which are predicted to have masses from $\mathcal{O}(10)$ GeV up to several TeV, with a theoretical upper limit of 340 TeV based on unitarity require-

ments [2]. Particles that have properties of a WIMP naturally arise from many theories, which were not initially designed for this purpose. For example, the neutralino in supersymmetric models or the lightest Kaluza-Klein particle in theories with extra dimensions are natural WIMP candidates.

WIMPs could self-annihilate if they are Majorana particles, or decay, resulting in stable particles like gamma-rays, electrons and neutrinos. A measurable flux of such particles would be strong indirect evidence for the existence of dark matter. Regions with suspected high density of dark matter are prominent targets for these indirect searches since a large dark matter density corresponds to a higher flux of detectable particles. Since galaxies are expected to be embedded in a halo of dark matter, the Galactic halo and Galactic Center are examples of such expected high density regions.

Self-annihilation of dark matter particles in the Galaxy is of particular interest since a WIMP search via the product particles is sensitive to the velocity-averaged self-

*Physics Department, South Dakota School of Mines and Technology, Rapid City, SD 57701, USA

[†]Los Alamos National Laboratory, Los Alamos, NM 87545, USA

[‡]also Sezione INFN, Dipartimento di Fisica, I-70126, Bari, Italy

[§]NASA Goddard Space Flight Center, Greenbelt, MD 20771, USA

annihilation cross-section $\langle\sigma_A v\rangle$ [3]. In this sense, such searches are complementary to direct searches or indirect searches from the Sun. Like the direct searches, the latter probes the WIMP-nucleon scattering cross-section, since dark matter would be captured gravitationally due to repetitive elastic scattering. While the analysis presented in this paper is based on a search for an excess neutrino flux from the direction of the Galactic Center, IceCube also published results from a search for dark matter in the Galactic halo [4], as well as the Sun [5].

A search for neutrino signals from dark matter annihilations has inherent advantages over searches using photons or charged cosmic rays since neutrinos may escape the production point and arrive at the detector unimpeded by absorption by matter or deflection by the magnetic field in the central region of the Galaxy.

B. Signal from Annihilating or Decaying Dark Matter

A description of the dark matter density in the Milky Way is essential for a calculation of the signal flux. There are various models that attempt to describe the distribution profile of dark matter in Milky Way-size galaxies. These models describe a dark matter halo with a spherically symmetric matter density, $\rho_{\text{DM}}(r)$, that peaks at the center of the galaxy and decreases with distance. Profiles based on N-body simulations [6] of cold dark matter tend to show a divergent density in the central region. On the other hand, profiles that rely on observations of low surface brightness galaxies dominated by dark matter imply a flat distribution in the central region [7, 8]. Despite large differences in the description of the central region, the models show a similar density behavior at large distances from the Galactic Center ($\gtrsim 8.5$ kpc).

Frequently considered models are the Navarro-Frenk-White (NFW) model [9], the Moore et al. model [10] and the Kravtsov et al. model [11]. We use the NFW profile as a benchmark for the analysis presented in this paper, with the very cuspy Moore profile and the Kravtsov profile, which is close to isothermal or cored profiles, as extreme cases. These models are compared in Fig. 1.

The NFW profile is given by

$$\rho_{\text{DM}}(r) = \frac{\rho_0}{\frac{r}{r_s} \left(1 + \frac{r}{r_s}\right)^2}, \quad (1)$$

with $r_s = 20$ kpc [9]. The normalization parameter, ρ_0 , is chosen so that the dark matter density at the orbital distance of the solar system ($R_{\text{SC}} = 8.5$ kpc) is the assumed local density $\rho_{\text{DM}}(R_{\text{SC}}) = 0.3 \text{ GeV cm}^{-3}$ [3]. The choice of parameters is consistent with a previous analysis [4] of signals from the outer halo based on data from IceCube in the 22-string configuration (IceCube-22).

The expected neutrino flux from self-annihilation of a WIMP of mass m_χ is proportional to the square of the dark matter density, ρ_{DM}^2 , integrated along the line of

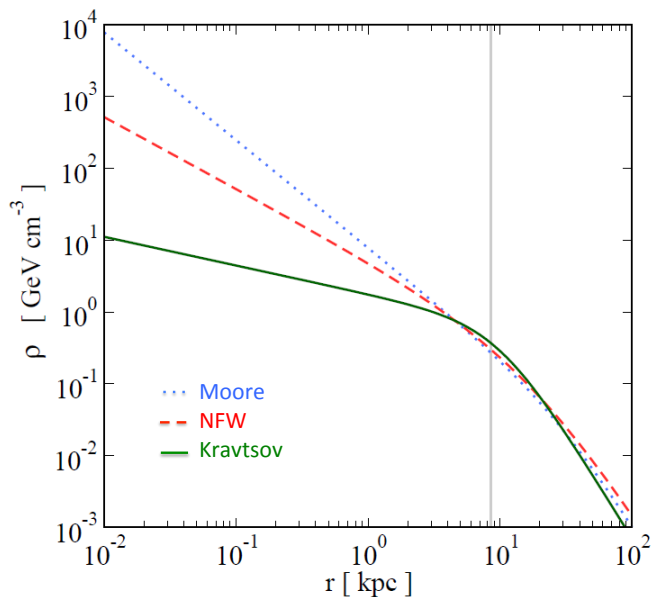


FIG. 1: Dark matter density as a function of the distance to the Galactic Center for three halo profiles [3]. From top to bottom, the Moore (blue-dotted), NFW (red-dashed) and Kravtsov (green-solid) profiles are shown. The vertical line marks the orbital radius of the solar system.

sight:

$$J_a(\Psi) = \int_0^{l_{\text{max}}} dl \frac{\rho_{\text{DM}}^2(\sqrt{R_{\text{SC}}^2 - 2lR_{\text{SC}}\cos\Psi + l^2})}{R_{\text{SC}}\rho_{\text{SC}}^2}. \quad (2)$$

Here Ψ is the angular distance of the line of sight with respect to the Galactic Center, and R_{SC} and $\rho_{\text{SC}} = \rho(R_{\text{SC}})$ are used as scaling parameters to make $J_a(\Psi)$ dimensionless. The upper limit of the integral is

$$l_{\text{max}} = \sqrt{R_{\text{MW}}^2 - \sin^2\Psi R_{\text{SC}}^2} + R_{\text{SC}}\cos\Psi, \quad (3)$$

where R_{MW} is the radius of the Milky Way dark matter halo. Typically, contributions from distances larger than the scale radius (r_s) of the halo model are sufficiently small and can be neglected [3]. A value of $R_{\text{MW}} = 40$ kpc is adopted in this analysis.

The quantity $J_{\Delta\Omega}$ is the average value of $J_a(\Psi)$ for a chosen search region. For a circular search region defined by the solid angle $\Delta\Omega$ it is described by

$$J_{\Delta\Omega} = \frac{2\pi \cdot \int_{\cos\Psi}^1 J_a(\Psi') d(\cos\Psi')}{\Delta\Omega}. \quad (4)$$

Figure 2 shows $J_a(\Psi)$ and $J_{\Delta\Omega}$ for the different halo models and a circular search region.

In the above scenario the neutrino flux at Earth has two possible components; annihilation or decay of dark

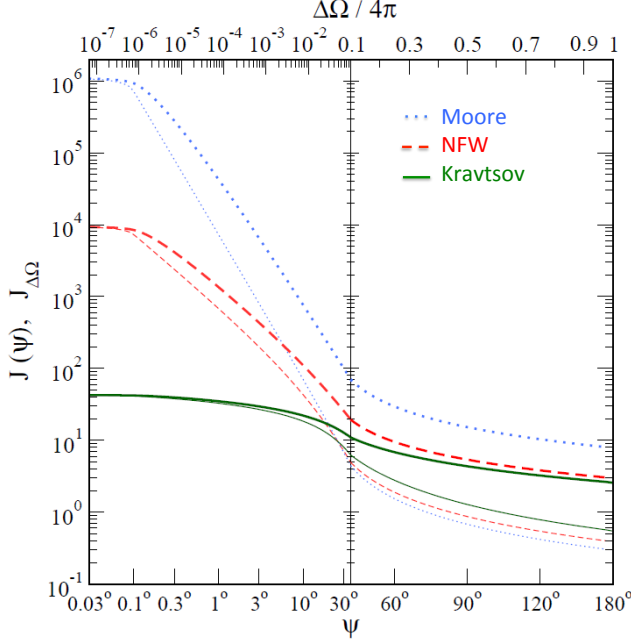


FIG. 2: The line of sight integral, $J_a(\Psi)$, and the average value of J_a for the solid angle defined by the opening angle, Ψ , as a function of Ψ [3]. The upper x-axis indicates the fraction of the solid angle defined by Ψ with respect to the full sphere. The thin lines show the value of J_a at an opening angle of Ψ while the thick lines depict $J_{\Delta\Omega}$ (which is the average value of J_a) in the cone defined by Ψ . The green (solid) lines show the Kravtsov profile, the red (dashed) lines show the NFW and the blue (dotted) lines corresponds to the Moore profile.

matter. The annihilation component may be written as [3]

$$\frac{d\phi_\nu}{dE} = \frac{\langle\sigma_A v\rangle}{2} J_a(\Psi) \frac{R_{sc}\rho_{sc}^2}{4\pi m_\chi^2} \frac{d\mathcal{N}_\nu}{dE}. \quad (5)$$

The $1/(4\pi)$ factor accounts for the isotropic radiation of the annihilation products and $d\mathcal{N}_\nu/dE$ gives the differential neutrino yield per annihilation. The factors ρ_{sc}/m_χ and R_{sc} normalize the dimensionless factor J_a to the number density, and the factor of $\frac{1}{2}$ accounts for the fact that two particles are required for annihilation.

The decay component is given by [12]

$$\frac{d\phi_\nu}{dE} = \frac{1}{\tau} J_d(\Psi) \frac{R_{sc}\rho_{sc}}{4\pi m_\chi} \frac{d\mathcal{N}_\nu}{dE}. \quad (6)$$

Here τ is the lifetime of the dark matter particle and $J_d(\Psi)$ is the line of sight integral over the dark matter density,

$$J_d(\Psi) = \int_0^{l_{\max}} dl \frac{\rho_{DM}(\sqrt{R_{sc}^2 - 2lR_{sc}\cos\Psi + l^2})}{R_{sc}\rho_{sc}}. \quad (7)$$

DARKSUSY [13] is used to obtain the neutrino energy spectra from WIMP-annihilations for various benchmark

annihilation channels and WIMP masses. Considered are specific masses of 100 GeV, 200 GeV, 300 GeV, 500 GeV, 700 GeV, 1 TeV, 2 TeV, 5 TeV and 10 TeV, and 100% branching into $b\bar{b}$, W^+W^- , $\mu^+\mu^-$ or $\tau^+\tau^-$ pairs. The obtained energy spectra represent a model-independent conversion of the WIMP mass to Standard Model particles and their subsequent decay. Therefore, the same spectra can be used for the calculation of lifetimes in the case of decaying dark matter.

Annihilation and decay to $\nu\bar{\nu}$ produce line spectra at the WIMP mass or half of the WIMP mass, respectively. The line spectrum is also interesting from a theoretical point of view as it can be used to obtain model-independent and conservative upper bounds for dark matter annihilation to Standard Model final states [14].

The choice of the annihilation channels cover a wide range of neutrino spectra. The $b\bar{b}$ channel gives a softer energy spectrum while $\mu^+\mu^-$ and $\nu\bar{\nu}$ channels provide a harder energy spectrum. For a specific supersymmetric scenario a superposition of these annihilation channels is expected, producing an effective neutrino energy spectrum that lies between the benchmark cases considered in this analysis.

The analysis presented here is based on a search for a muon-neutrino signal. For the calculation of the muon-neutrino flux at Earth all neutrino flavors are considered assuming a full mixing at Earth ($\nu_e : \nu_\mu : \nu_\tau = 1:1:1$) due to long-baseline oscillations:

$$\phi_{\nu_\mu} = \frac{1}{3} \sum_i \phi_{\nu_i}^0. \quad (8)$$

Here, $\phi_{\nu_i}^0$ is the initial flux at source for each flavor. Specific deviations from this benchmark assumption for vacuum oscillations, e.g. as described in [15] ($\theta_{23} \approx \pi/4, \theta_{13} \approx 0, \sin^2(2\theta_{12}) = 0.86$), lead to small changes in the predicted fluxes at the few percent level.

Figure 3 shows the expected energy distribution of muon-neutrinos after full mixing at Earth for different annihilation channels of a 300 GeV WIMP. Annihilation to $\nu\bar{\nu}$ produces a line spectrum at the WIMP mass.

The expected number of neutrino events is found by integrating equations (5) or (6) over the detector live-time and the direction- and energy-dependent effective area for annihilation or decay, respectively. This procedure permits the direct conversion of an observed flux at the detector to the velocity-averaged self-annihilation cross-section $\langle\sigma_A v\rangle$, or the WIMP lifetime τ .

C. The IceCube-40 Detector

The IceCube in-ice neutrino detector is a cubic-kilometer array of digital optical modules (DOMs) deployed between 1450 m and 2450 m below the surface in the glacial ice of the South Pole. Each DOM consists of a glass pressure housing enclosing a 25,4 cm diameter Hamamatsu photomultiplier tube with digitizing electronics, and a set of LEDs for calibration [16, 17]. The

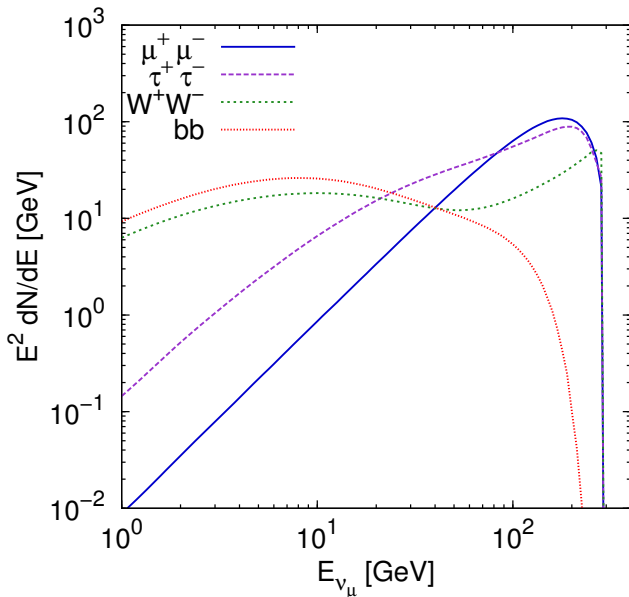


FIG. 3: Energy spectra at Earth for different annihilation channels, including neutrino oscillations, for a 300 GeV WIMP. The spectra were obtained with DARKSUSY [13].

DOMs are autonomous data collection units with a time resolution of less than 3 ns [18]. They detect Cherenkov light emitted by the medium due to interaction with relativistic charged particles, including charged leptons produced in neutrino interactions in the ice, and muons produced by cosmic-ray interactions in the atmosphere.

The complete in-ice detector consists of 5160 DOMs deployed on 86 strings (60 DOMs per string). Here 78 of the strings are arranged in a triangular pattern and form a nearly hexagonal grid with 125 m inter-string spacing and 17 m vertical DOM separation. The remaining 8 strings are located near the center of the detector interspersed with the standard IceCube strings, and have an average inter-string separation of 72 m and vertical DOM spacing of 7 m. Together with the surrounding 6 IceCube strings and the central string, these strings form the low-energy sub-array called DeepCore [19], which is of particular interest for dark matter searches due to the lower energy threshold.

The construction of IceCube was completed in December 2010, but the detector was operational during the construction period from 2005 to 2010. In this paper we use data from the 40-string configuration of IceCube (IceCube-40, see Fig. 4) collected between April 2008 and May 2009, when IceCube did not contain any DeepCore strings.

The IceCube-40 data acquisition system applied several trigger algorithms designed to collect different event topologies. This analysis considers events that satisfy the SMT8 trigger, a simple multiplicity trigger, requiring at least 8 DOMs to record a signal above threshold within a time window of $5 \mu\text{s}$ [17].

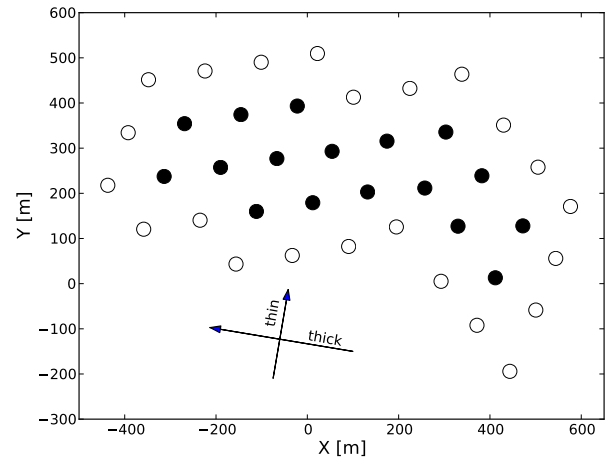


FIG. 4: A sketch of string locations for the IceCube-40 detector (top view). The outer strings (open circles), which are used as a veto, as well as defined directions labeled as thick and thin are marked.

D. Dataset and Analysis

The data used represents 367 days of detector live-time [20]. Given IceCube’s location at the South Pole, any search for a neutrino flux from the direction of the Galactic Center, located in the southern sky (RA $17^h 45^m 40.04^s$, Dec $-29^\circ 00' 28.1''$), is impacted by a significant background of cosmic-ray induced atmospheric muons and atmospheric neutrinos. The analysis strategy is to identify and select neutrino events which have an interaction vertex inside the detector volume, since atmospheric muons, the dominant background, must enter from outside. The large instrumented volume of IceCube-40 allows the definition of a veto region, while retaining a sufficiently large fiducial volume for starting events. The upper thirty DOMs on each string define a *top-veto* while the complete strings in the outer layer of IceCube-40 form a *side-veto* (Fig. 4). Events with one or more hit in the top veto or with the earliest hit recorded on any of the outer strings, are rejected.

Events surviving the veto condition are reconstructed with an iterative log-likelihood track reconstruction method [21]. Based on the initial direction reconstruction, only events with a zenith angle larger than 50° and an azimuth direction between 135° to 225° and 300° to 30° , angular regions corresponding to the axis labeled as “thick” in Fig. 4, are selected. For events outside these regions the detector is not thick enough to define an efficient veto. Further cuts are applied to improve the angular resolution of the data. Examples of such cuts include the reduced log-likelihood value from a track reconstruction or the number of strings that have registered a hit in the recorded event.

To identify events with a neutrino interaction vertex within the detector a likelihood algorithm has been de-

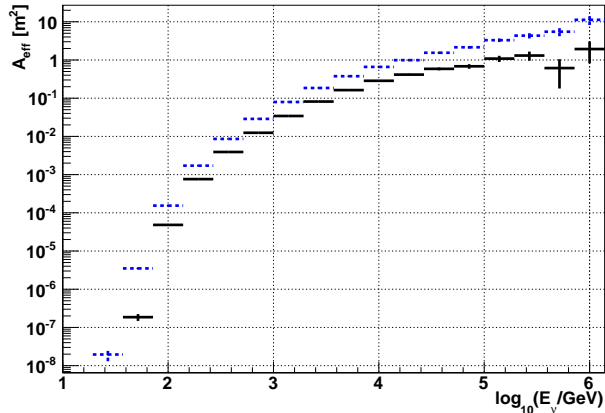


FIG. 5: Effective area for neutrinos from MonteCarlo simulation for the direction of the Galactic Center after application of the veto conditions and angular cuts (blue-dashed) and after subsequent application of quality and signal selection cuts (black-solid).

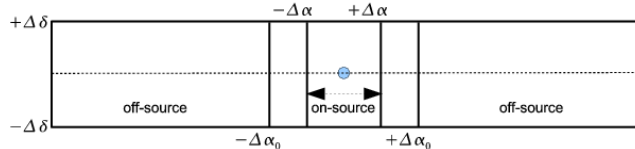


FIG. 6: Definition of the on-source and off-source regions. The extent of the declination band is $2\Delta\delta$ for all regions. The width of the on-source region in right ascension is $2\Delta\alpha$. The region between $\Delta\alpha$ and $\Delta\alpha_0$ is used as buffer. The region beyond $\Delta\alpha_0$ is defined as off-source. In this analysis values of $\Delta\delta = 8^\circ$, $\Delta\alpha = 9^\circ$, and $\Delta\alpha_0 = 20^\circ$ are used.

veloped that analyzes the event topology [20]. This algorithm determines the likelihood of a muon to produce or not produce hits in the DOMs along the reconstructed track up-stream of an assumed starting point and it includes the optical properties of the ice. Maximizing the likelihood gives the location of the interaction vertex. The likelihood ratio of a starting track relative to a through-going track hypothesis is used as a classifier to further reduce the atmospheric muon background.

The above-mentioned quality and signal selection cuts reduce the dataset by about two orders of magnitude. The event rate is reduced from an initial trigger rate of about 1 kHz (SMT8) to 2 Hz (initial veto and azimuth cuts) to 0.56 Hz (quality and signal selection cuts). Figure 5 shows the effective area of the detector before and after the event quality selection. The median angular resolution at this level is about 2.6° . The data remains dominated by cosmic-ray muons, undetected in the veto region, that enter the detector from outside.

This analysis uses an on-source/off-source method, as shown in Fig. 6, to estimate the background directly from the data. The highest flux of WIMP annihilation prod-

ucts is expected to arrive from the direction of a wide region centered at the Galactic Center. The atmospheric muon and neutrino background at the location of IceCube varies with the zenith (or declination) angle but is approximately constant in right ascension. Therefore, events from a declination band around the Galactic Center were selected. The width of the band in declination, $\pm\Delta\delta$, was optimized by maximizing S/\sqrt{B} , where S and B are the number of expected signal and background events respectively for each WIMP mass and each annihilation channel. Optimal bin sizes for $\Delta\delta$ were found to be between 6° and 8° . The variation of S/\sqrt{B} with $\Delta\delta$ is rather small and a value of $\Delta\delta = 8^\circ$ was adopted for all WIMP masses and annihilation channels.

The on-source region width in right ascension, $\Delta\alpha$, is chosen to be equal to the size of the on-source region in declination at the zenith angle of the Galactic Center:

$$\cos \Delta\alpha = \frac{\cos(\Delta\delta) - \cos^2(\theta_{GC})}{\sin^2(\theta_{GC})}, \quad (9)$$

where θ_{GC} is the zenith angle of the Galactic Center in local coordinates (61°). This yields a value for $\Delta\alpha \approx 9^\circ$. No sharp transition between on- and off-source regions exists because the dark matter density profile decreases continuously with distance from the Galactic Center. To reduce the signal contamination of the background estimate from the off-source region, we define a buffer between the on-source region and the off-source region (Fig. 6). An event is considered off-source, and thus used for the background estimate, if the angular distance to the Galactic Center is $\Delta\alpha_0 \geq 20^\circ$. Events between $\Delta\alpha_0$ and $\Delta\alpha$ are discarded.

The expected number of background events in the on-source region, N_{BG}^{on} , is:

$$N_{BG}^{on} = N_{BG}^{off} \cdot \frac{\Delta\alpha}{180^\circ - \Delta\alpha_0}, \quad (10)$$

where N_{BG}^{off} is the number of background events in the off-source region. This method of background estimation relies on measured data and is therefore independent of Monte Carlo simulations and related systematic uncertainties (e.g. modeling of optical ice properties or the detector response).

Despite the daily rotation of the detector variations of up to 1.5% are found in the right ascension distribution of the final event selection (Fig. 7). The origin of these variations is the non-uniform azimuthal acceptance, caused by the asymmetric geometrical layout of IceCube-40, combined with periods of detector inactivity which are not evenly distributed in time. The arising uncertainty is larger than the expected statistical uncertainty on the background estimate. A procedure has been applied to account for the uneven exposure:

- First, we determine the normalized distribution, $D(\phi)$, of all measured event azimuth angles, ϕ , in detector coordinates that do not originate in

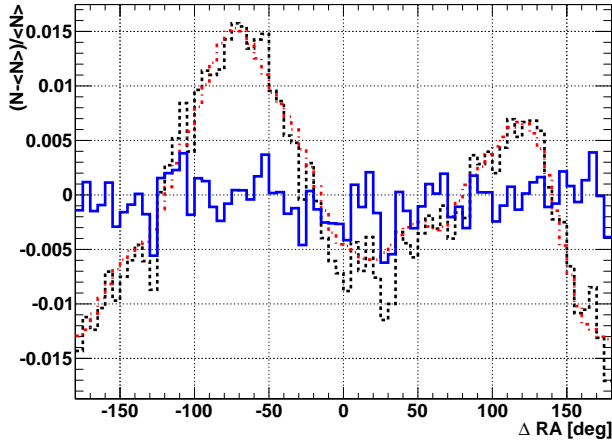


FIG. 7: Relative variation of the event distribution in RA (with respect to the Galactic Center, thus the x-axis is labeled ΔRA). N is the number of measured events per bin, $\langle N \rangle$ is the average number of events in all bins. The measured (black-dotted) and expected (red-dashed-dotted) distributions are shown, along with the deviation from expectation (blue).

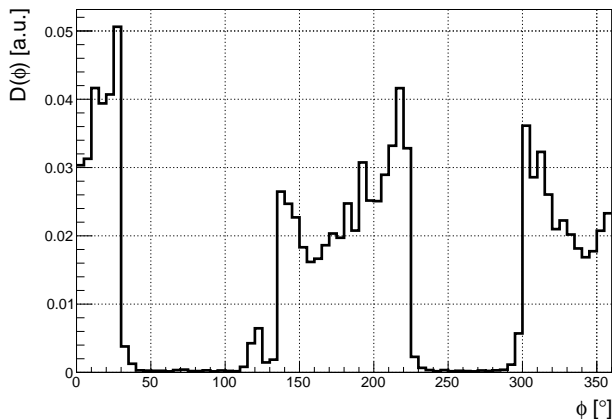


FIG. 8: Initial azimuth pdf containing all events from the off-source region. The cuts on the reconstructed azimuth were performed on an initial reconstruction. This figure shows the azimuth distribution based on an advanced reconstruction. The cut regions excluding events from the “thin” (Fig. 4) detector orientation are clearly visible.

the on-source region. This distribution, shown in Fig. 8, corresponds to the effective probability density function (pdf) for the observation of an event from a certain detector direction, integrated over the exposure in time. This pdf rotates with the detector and is not the exposure in right ascension.

- Second, we transform for each event time the full pdf to equatorial coordinates (RA, δ): $D'_i(RA) = D(RA + \Delta\phi_i)$. At IceCube’s location, this corre-

TABLE I: $J_{\Delta\Omega}$ for annihilating dark matter for the considered halo density profiles and the chosen on-source region.

	NFW	Kravtsov	Moore
$J_{\Delta\Omega}$	240	23	900

sponds to a rotation of the azimuth pdf by an angle, $\Delta\phi_i$, that can be calculated from the event time.

- Lastly, we calculate the sum of all the obtained distributions (in RA):

$$D'(RA) = \sum_i^N D'_i = \sum_i^N D(RA + \Delta\phi_i), \quad (11)$$

where N is the total number of events.

The application of this procedure results in an exposure-corrected expected distribution of background events in right ascension, normalized to the number of events in the full dataset. Figure 7 shows the accuracy of the number of predicted events. The agreement between the number of measured and expected events is at the 0.1 %-level. This approach also takes seasonal variations into account.

E. Systematic Uncertainties

Predictions of the expected signal are dominated by large variations in the description of the central region of halo models (Fig. 1). In particular, in the direction of the Galactic Center, the line of sight integral, $J(\Psi)$, spans several orders of magnitude (Fig. 2). For this reason we have chosen the NFW profile as a benchmark model, and do not consider the halo-model dependence a systematic uncertainty.

The limits obtained in this analysis can be rescaled to limits for the Moore or Kravtsov profile by multiplication of the limit for each mass or channel with $J_{\Delta\Omega}^{NFW}/J'_{\Delta\Omega}$, where $J'_{\Delta\Omega}$ is the desired profile. The corresponding values of $J_{\Delta\Omega}$ were obtained for the actual box-shaped search bin (not by means of equation (4)) and are shown in Table I. However, especially for flat-cored profiles the signal-contamination of the off-source region has to be considered when rescaling the limits.

The background prediction is derived from the high-statistics off-source data sample. The systematic uncertainty in this prediction is limited to small directional variations in the cosmic ray flux, e.g. as reported in [22]. A Kolmogorov-Smirnov test for compatibility of the relative deviations to a normal distribution yields a p-value of 0.77. Within the limited statistics of 72 values (5°-bins), the result does not hint at a possible anisotropy in this data sample.

Though the background estimate is data-driven, systematic uncertainties arise from the Monte Carlo-based estimation of the detector sensitivity for signal events. Typically, the energies considered in this analysis are

TABLE II: Summary of systematic effects.

Effect	Contribution
live-time	< 1 %
ν cross-section and propagation	7 %
photon propagation and optical ice properties	20 %-25 %
total (conservative)	33 %

lower than for other IceCube analyses, e.g. the search for high energy extragalactic neutrinos, and are largely similar to the energies considered in Ref. [4, 5]. For lower energies, the uncertainties on the neutrino cross-section and neutrino and muon propagation are on the order of 7 % [5]. In addition, uncertainties corresponding to the detector up-time are less than 1%. Uncertainties related to the detection efficiency of low energy events, such as the sensitivity of optical modules [16] and the photon propagation through the ice [23], are considerably larger. These effects lead to a typical uncertainty on the total effective area of about 25 % for lower energies, $\mathcal{O}(100 \text{ GeV})$, and about 20 % for energies near 1 TeV. Though the impact of the above-mentioned systematics is energy-dependent we conservatively assume a 33 % effect on the signal detection efficiency, ϵ_{det} . Here, ϵ_{det} corresponds to the integration over energy of the neutrino multiplicity per annihilation multiplied by the effective area:

$$\epsilon_{\text{det}} \propto \int dE A_{\text{eff}}(E) \frac{dN_\nu}{dE}. \quad (12)$$

The value of 33 % is propagated into the limits by means of equation (5),

$$\langle \sigma_A v \rangle \propto \frac{N_{\text{lim}}}{\epsilon_{\text{det}} \cdot (1 \pm 0.33)}, \quad (13)$$

for all channels and masses, where N_{lim} is the limit on the number of signal neutrinos in the sample. The systematic uncertainty on the lifetimes have been included by means of equation (6),

$$\tau \propto \frac{\epsilon_{\text{det}} \cdot (1 \pm 0.33)}{N_{\text{lim}}}. \quad (14)$$

The presented limits have been shifted upwards by a factor of 1/0.67 to include systematic effects in a conservative way.

F. Results

The number of observed events in the on-source region was $N^{\text{on}} = 798\,842$, while $N_{\text{BG}}^{\text{on}} = 798\,819$ background events were expected based on estimates from the approximately 5 times larger off-source region, using equation (10). This procedure yields a relatively

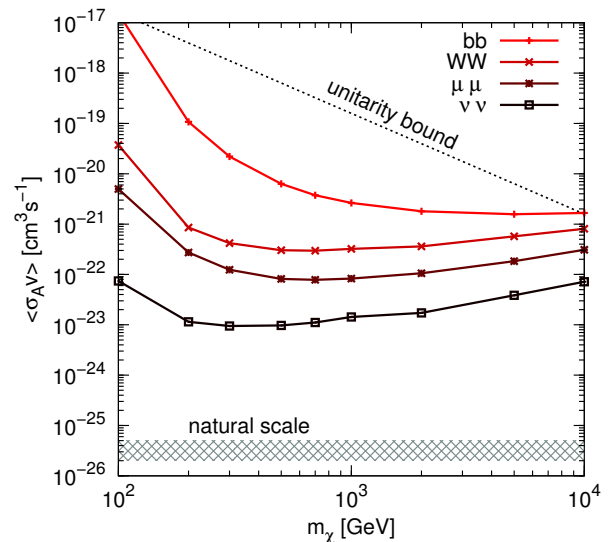


FIG. 9: Upper limits (90 % C.L.) on the self-annihilation cross-section for the four channels at nine WIMP masses. The hashed area represents the natural scale at which WIMPs are thermal relics [25]. The black-dotted line is the unitarity bound [2, 26]. The four limits were derived assuming the NFW density profile.

small uncertainty on the background expectation. If the null hypothesis is valid, the outcome of a large number of measurements of N^{on} is expected to follow a Poisson distribution around $N_{\text{BG}}^{\text{on}}$. The small difference of $\Delta N = N^{\text{on}} - N_{\text{BG}}^{\text{on}} = 23$ events, compared to a standard deviation of about 916 events, is compatible with no neutrino signal from annihilations of dark matter particles. Based on Feldman-Cousins [24], an upper limit (90 % C.L.) of 1504 signal neutrinos is computed. From equation (5), the limit on the velocity-averaged WIMP self-annihilation cross-section $\langle \sigma_A v \rangle$ for annihilations in the Galactic Center is derived for various WIMP masses and annihilation channels (Fig. 9). Similarly, with equation (6), lower limits on the WIMP lifetime are calculated (Fig. 10).

G. Comparison with Results from Other Indirect Searches

Several satellite-borne and balloon experiments have reported deviations of measured cosmic-lepton spectra from theoretical predictions. The PAMELA collaboration observed an increased positron fraction at energies above $\sim 10 \text{ GeV}$ [28], that disagrees with the conventional model for cosmic-rays [29] (secondary positron production only). This measurement has also been confirmed by the Fermi-LAT collaboration [30]. Further, the Fermi-LAT [31] and HESS [32, 33] measurements of primary electrons showed a discrepancy when compared to conventional diffuse models. Though the results

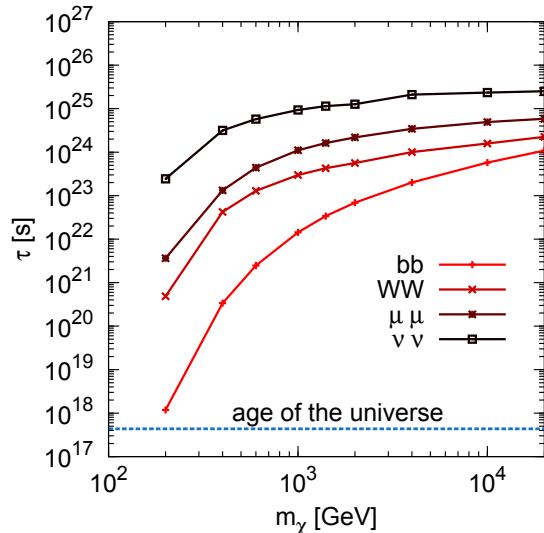


FIG. 10: Lower limits (90 % C.L.) on the lifetime for the four channels at nine WIMP masses. The horizontal line represents the age of the universe [27]. The four limits were derived assuming the NFW density profile.

may be interpreted as signals from nearby astrophysical sources [34], they could also be explained by annihilation or decay of leptophilic dark matter with a mass of $\mathcal{O}(1 \text{ TeV})$. With this assumption, preferred regions in the $\langle\sigma_A v\rangle$ - m_χ -plane can be identified [35, 36] and compared to the limits obtained in this analysis. Figure 11 shows our $\mu^+\mu^-$ channel limits compared to those regions. Figure 12 shows a similar comparison for the $\tau^+\tau^-$ channel where the current limits are close to the preferred regions of the combined PAMELA and Fermi data. The better exclusion power in the τ -channel is not due to a more stringent limit, but rather the location of the favored regions since there is significant energy loss during electron propagation, any electron or positron signal must originate from nearby sources ($\mathcal{O}(1 \text{ kpc})$). Given this, the shape of the preferred regions does not depend strongly on the halo profile.

Recently, the Fermi-LAT collaboration [37] reported results from a search for dark matter annihilation signals from 10 dwarf galaxies. For gamma-ray experiments dwarf galaxies are very promising targets due to a relatively high signal-to-noise ratio. The obtained limits are very stringent and a comparison to our Galactic Center limits, as well as the IceCube-22 Galactic halo limits [4], is shown in Fig. 13. At lower WIMP masses the dwarf limits are more constraining than the IceCube limits by several orders of magnitude. However, the IceCube limits on direct annihilation to neutrinos can be regarded as a very conservative bound on the total dark matter annihilation to Standard Model final states [14]. At higher WIMP masses ($\geq \text{TeV}$), where there is larger neutrino cross-section and muon range, IceCube benefits from the large instrumented volume due to the increasing neutrino

cross-section and the muon range [38].

In a different approach, the dark matter self-annihilation cross-section can also be constrained based on precise measurement of the cosmic microwave background (CMB). A too large self-annihilation cross-section can cause significant distortions of the CMB depending on the annihilation mode. The lack of such distortions can be translated to a limit on $\langle\sigma_A v\rangle$.

Very stringent limits were obtained [39, 40] from measurements of temperature, anisotropy and polarization of the CMB, based on WMAP [27] and ACT [41] data.

We refrain from comparing the derived limits to our results as our analysis targets dark matter properties in the present epoch, while conditions in the early universe were substantially different, e.g. the velocity distribution, as well as the energy absorption processes in the photon-baryon plasma [42].

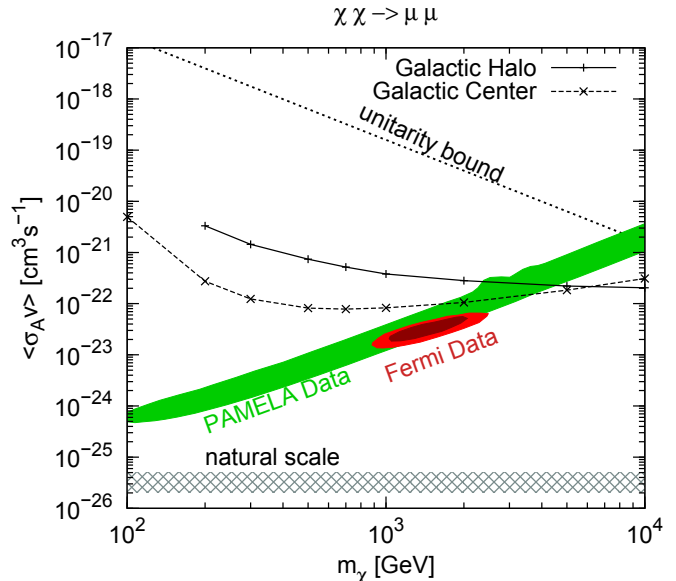


FIG. 11: Upper limits (90 % C.L.) on the self-annihilation cross-section for the annihilation channel to muons at nine WIMP masses assuming the NFW density profile (solid line). The hashed area represents the natural scale at which WIMPs are thermal relics [25]. The black-dotted line is the unitarity bound [2, 26]. The green (3σ) region is based on the PAMELA excess, the red region represents the PAMELA data combined with the Fermi and H.E.S.S. data (3σ and 5σ) [35].

H. Summary and Outlook

The analysis of IceCube data in the 40-string configuration has been presented and yields limits for a wide range of WIMP masses and annihilation channels. Figure 13 shows the limits from this analysis compared to those from an analysis of the outer halo with IceCube-22 [4]. Roughly an order of magnitude improvement has

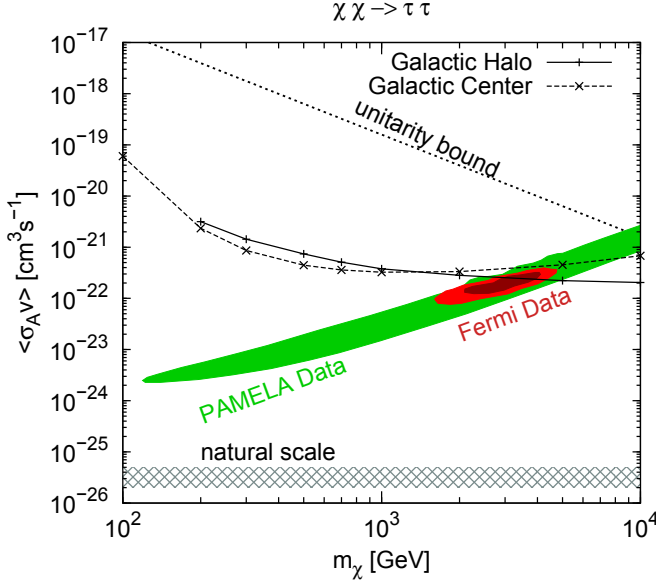


FIG. 12: Upper limits (90 % C.L.) on the self-annihilation cross-section for the annihilation channel to tau leptons at nine WIMP masses assuming the NFW density profile (solid line). The hashed area represents the natural scale at which WIMPs are thermal relics [25]. The black-dotted line is the unitarity bound [2, 26]. The green (3σ) region is based on the PAMELA excess, the red region represents the PAMELA data combined with the Fermi and H.E.S.S. data (3σ and 5σ) [35].

been achieved in the lower mass range, while at higher masses neutrino limits provide some of the most stringent constraints. Further, neutrino constraints can be used to test scenarios motivated by the anomalous lepton observations and are also extremely effective in ruling out scenarios for high mass WIMPs. Recent Fermi observations of diffuse gamma-ray flux could hint at such scenarios, in which the unitarity bound does not apply, for example in p-wave dominated annihilation scenarios, or models of composite dark matter [43].

The sensitivity of this analysis is limited by the significant atmospheric muon background in direction of the Galactic Center as well as the relatively high detection threshold. Substantial improvement is expected from analyses using the considerably larger detector configuration with 79 strings, IceCube-79, and the complete IceCube-86 detector. A larger detector provides a larger fiducial volume while maintaining a sufficiently large and effective veto volume to suppress the atmospheric background [44]. In addition, preliminary estimates suggest that the DeepCore low-energy extension, first present in IceCube-79, increases the effective area significantly in the energy region between 10 GeV and 100 GeV. Dedicated data filters for the Galactic Center have been developed and implemented for IceCube-79 [38], and further improved in terms of signal acceptance for the complete IceCube-86 detector.

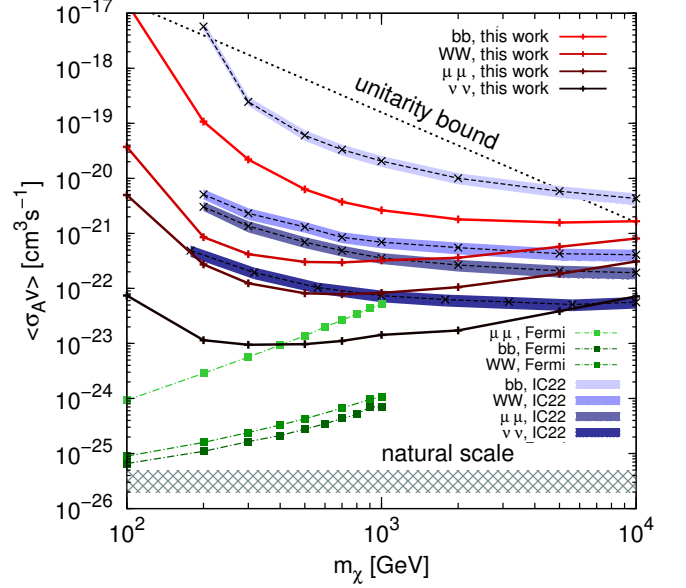


FIG. 13: The upper limits from this analysis compared to those from an analysis of the outer Galactic halo using IceCube-22 data [4], as well as limits obtained from observation of dwarf galaxies by the Fermi-LAT collaboration [37].

Acknowledgments

We acknowledge the support from the following agencies: U.S. National Science Foundation-Office of Polar Programs, U.S. National Science Foundation-Physics Division, University of Wisconsin Alumni Research Foundation, the Grid Laboratory Of Wisconsin (GLOW) grid infrastructure at the University of Wisconsin - Madison, the Open Science Grid (OSG) grid infrastructure; U.S. Department of Energy, and National Energy Research Scientific Computing Center, the Louisiana Optical Network Initiative (LONI) grid computing resources; National Science and Engineering Research Council of Canada; Swedish Research Council, Swedish Polar Research Secretariat, Swedish National Infrastructure for Computing (SNIC), and Knut and Alice Wallenberg Foundation, Sweden; German Ministry for Education and Research (BMBF), Deutsche Forschungsgemeinschaft (DFG), Research Department of Plasmas with Complex Interactions (Bochum), Germany; Fund for Scientific Research (FNRS-FWO), FWO Odysseus programme, Flanders Institute to encourage scientific and technological research in industry (IWT), Belgian Federal Science Policy Office (Belspo); University of Oxford, United Kingdom; Marsden Fund, New Zealand; Australian Research Council; Japan Society for Promotion of Science (JSPS); the Swiss National Science Foundation (SNSF), Switzerland.

-
- [1] G. Bertone, D. Hooper, and J. Silk, *Phys. Rept.* **405**, 279 (2005), arXiv:0404175 [hep-ph].
 - [2] K. Griest and M. Kamionkowski, *Phys. Rev. Lett.* **64**, 615 (1990).
 - [3] H. Yuksel, S. Horiuchi, J. F. Beacom, and S. Ando, *Phys. Rev.* **D76**, 123506 (2007), arXiv:0707.0196 [astro-ph].
 - [4] R. Abbasi et al. (IceCube Collaboration), *Phys. Rev.* **D84**, 022004 (2011), arXiv:1101.3349 [astro-ph].
 - [5] R. Abbasi et al. (IceCube Collaboration), *Phys. Rev. D* **85**, 042002 (2012).
 - [6] J. Diemand, M. Kuhlen, and P. Madau, *Astrophys. J.* **667**, 859 (2007), arXiv:0703337 [astro-ph].
 - [7] W. J. G. De Blok, A. Bosma, and S. McGaugh (IceCube Collaboration), *Monthly Notices of the Royal Astronomical Society* **340**, 657 (2003), ISSN 1365-2966.
 - [8] W. J. G. de Blok (2009), arXiv:0910.3538 [astro-ph].
 - [9] J. F. Navarro, C. S. Frenk, and S. D. M. White, *Astrophys. J.* **462**, 563 (1996), arXiv:9508025 [astro-ph].
 - [10] B. Moore et al., *Astrophys. J.* **524**, L19 (1999).
 - [11] A. V. Kravtsov, A. A. Klypin, J. S. Bullock, and J. R. Primack, *Astrophys. J.* **502**, 48 (1998), arXiv:9708176 [astro-ph].
 - [12] H. Yuksel and M. D. Kistler, *Phys. Rev. D* **78**, 023502 (2008).
 - [13] P. Gondolo et al., *JCAP* **0407**, 008 (2004), arXiv:0406204 [astro-ph].
 - [14] J. F. Beacom, N. F. Bell, and G. D. Mack, *Phys. Rev. Lett.* **99**, 231301 (2007), arXiv:0608090 [astro-ph].
 - [15] G. Barenboim and C. Quigg, *Phys. Rev. D* **67**, 073024 (2003).
 - [16] R. Abbasi et al. (IceCube Collaboration), *Nucl. Instr. Meth. A* **618**, 139 (2010), arXiv:1002.2442 [astro-ph].
 - [17] R. Abbasi et al. (IceCube Collaboration), *Nucl. Instrum. Meth. A* **601**, 294 (2009), arXiv:0810.4930 [physics.ins-det].
 - [18] A. Achterberg et al. (IceCube Collaboration), *Astropart. Phys.* **26**, 155 (2006), astro-ph/0604450.
 - [19] R. Abbasi et al., *Astroparticle Physics* **35**, 615 (2012), ISSN 0927-6505.
 - [20] J. P. Huelss, Ph.D. thesis, RWTH Aachen University (2010).
 - [21] J. Ahrens et al. (AMANDA Collaboration), *Nucl. Instr. Meth. A* **524**, 169 (2004).
 - [22] R. Abbasi et al. (IceCube Collaboration), *The Astrophysical Journal* **740**, 16 (2011).
 - [23] M. Ackermann et al. (AMANDA Collaboration), *J. Geophys. Res.* **111**, D13203 (2006).
 - [24] G. J. Feldman and R. D. Cousins, *Phys. Rev.* **57**, 3873 (1998).
 - [25] G. Steigman, B. Dasgupta, and J. F. Beacom (2012), arXiv:1204.3622 [hep-ph].
 - [26] L. Hui, *Phys. Rev. Lett.* **86**, 3467 (2001), arXiv:0102349 [astro-ph].
 - [27] N. Jarosik et al., *Astrophys. J. Suppl.* **192**, 14 (2011), arXiv:1001.4744 [astro-ph].
 - [28] O. Adriani et al. (PAMELA Collaboration), *Nature* **458**, 607 (2009), arXiv:0810.4995 [astro-ph].
 - [29] I. V. Moskalenko and A. W. Strong, *Astrophys. J.* **493**, 694 (1998), arXiv:9710124 [astro-ph].
 - [30] M. Ackermann et al. (Fermi-LAT Collaboration), *Phys. Rev. Lett.* **108**, 011103 (2012).
 - [31] A. A. Abdo et al. (Fermi-LAT Collaboration), *Phys. Rev. Lett.* **102**, 181101 (2009), arXiv:0905.0025 [astro-ph].
 - [32] F. Aharonian et al. (H.E.S.S. Collaboration), *Astron. Astrophys.* **508**, 561 (2009), arXiv:0905.0105 [astro-ph].
 - [33] F. Aharonian et al. (H.E.S.S. Collaboration), *Phys. Rev. Lett.* **101**, 261104 (2008).
 - [34] H. Yuksel, M. D. Kistler, and T. Stanev, *Phys. Rev. Lett.* **103**, 051101 (2009), arXiv:0810.2784 [astro-ph].
 - [35] P. Meade, M. Papucci, A. Strumia, and T. Volansky, *Nucl. Phys.* **B831**, 178 (2010), arXiv:0905.0480 [hep-ph].
 - [36] M. Cirelli, M. Kadastik, M. Raidal, and A. Strumia, *Nucl. Phys.* **B813**, 1 (2009), arXiv:0809.2409 [hep-ph].
 - [37] M. Ackermann et al. (Fermi-LAT Collaboration), *Phys. Rev. Lett.* **107**, 241302 (2011).
 - [38] R. Abbasi et al. (IceCube Collaboration) (2011), arXiv:1111.2738 [astro-ph].
 - [39] S. Galli, F. Iocco, G. Bertone, and A. Melchiorri, *Phys. Rev. D* **80**, 023505 (2009).
 - [40] S. Galli, F. Iocco, G. Bertone, and A. Melchiorri, *Phys. Rev. D* **84**, 027302 (2011).
 - [41] J. W. Fowler et al., *The Astrophysical Journal* **722**, 1148 (2010).
 - [42] T. R. Slatyer, N. Padmanabhan, and D. P. Finkbeiner, *Phys. Rev. D* **80**, 043526 (2009).
 - [43] K. Murase and J. F. Beacom (2012), 1206.2595.
 - [44] S. Euler, D. Grant, and O. Schulz (IceCube Collaboration), *Proc. 31st ICRC OG2.5* (2009).